



This is a repository copy of *Low-dimensional emissive states in non-stoichiometric methylammonium lead halide perovskites*.

White Rose Research Online URL for this paper:
<http://eprints.whiterose.ac.uk/145964/>

Version: Accepted Version

Article:

Freestone, B.G. orcid.org/0000-0003-4436-8598, Smith, J.A. orcid.org/0000-0001-6889-4408, Piana, G. et al. (12 more authors) (2019) Low-dimensional emissive states in non-stoichiometric methylammonium lead halide perovskites. *Journal of Materials Chemistry A*, 7. pp. 11104-11116. ISSN 2050-7488

<https://doi.org/10.1039/c8ta12184b>

© The Royal Society of Chemistry 2019. This is an author-produced version of a paper subsequently published in *Journal of Materials Chemistry A*. Uploaded in accordance with the publisher's self-archiving policy.

Reuse

Items deposited in White Rose Research Online are protected by copyright, with all rights reserved unless indicated otherwise. They may be downloaded and/or printed for private study, or other acts as permitted by national copyright laws. The publisher or other rights holders may allow further reproduction and re-use of the full text version. This is indicated by the licence information on the White Rose Research Online record for the item.

Takedown

If you consider content in White Rose Research Online to be in breach of UK law, please notify us by emailing eprints@whiterose.ac.uk including the URL of the record and the reason for the withdrawal request.



eprints@whiterose.ac.uk
<https://eprints.whiterose.ac.uk/>

Low-dimensional emissive states in non-stoichiometric methylammonium lead halide perovskites

Benjamin G. Freestone¹, Joel A. Smith¹, Giacomo Piana², Rachel C. Kilbride¹, Andrew J. Parnell¹, Luca Sortino¹, David M. Coles¹, Orianna B. Ball¹, Natalia Martsinovich³, Courtney Thompson³, Tarek I. Alanazi¹, Onkar S. Game¹, Alexander I. Tartakovskii¹, Pavlos Lagoudakis² and David G. Lidzey^{1*}

¹ *Department of Physics and Astronomy, University of Sheffield, Sheffield, S3 7RH, U.K.*

² *Department of Physics and Astronomy, University of Southampton, SO17 1BJ, U.K.*

³ *Department of Chemistry, University of Sheffield, S3 7RH, U.K.*

* *Corresponding author: Prof. David G. Lidzey, d.g.lidzey@sheffield.ac.uk*

◦ *These authors contributed equally to this work*

Mixed-halide perovskites prepared from methylammonium iodide and lead chloride (MAPbI_{3-x}Cl_x) precursors are becoming increasingly well understood, however the effect of non-stoichiometry in this system is still not clear. Here, we create MAPbI_{3-x}Cl_x perovskites from starting mixtures containing an excess of MAI, and study them using a variety of structural and optical probes. Using grazing incidence X-ray scattering (GIWAXS) we demonstrate the existence of non-perovskite structures, and show that addition of hydroiodic acid (HI) also leads to similar low-dimensional phase formation. Photoluminescence spectroscopy performed at cryogenic temperatures indicates the existence of multiple emissive states between 510 nm and 605 nm resulting from a low dimensional phase (LDP) or multiple phases. By mapping the distribution of luminescence across the surface with submicron resolution, we found strong co-localisation of LDP emissive states. At certain blend ratios, emission is seen from both LDP states and methylammonium lead iodide perovskite (around 770 nm). Photoluminescence excitation spectroscopy of mixed-phase films reveals energy transfer, or a cascade, between different LDP states, but this process only occurs inefficiently to the surrounding perovskite. Time-resolved photoluminescence measurements demonstrate that LDP excited-state lifetimes decrease as a function of increasing temperature; a process consistent with a thermally-activated charge transfer process. Our work suggests that non-stoichiometric materials prepared via this processing route can lead to the formation of metastable LDPs with unique material properties that merit further investigation.

1 Introduction

Perovskite semiconductors have attracted worldwide interest since the first use of a methylammonium ($\text{MA} = \text{CH}_3\text{NH}_3^+$) lead-halide perovskite MAPbX_3 ($\text{X} = \text{Cl}^-$, Br^- or I^-) in a dye-sensitised solar cell.¹ The ease by which hybrid organic-inorganic perovskites can be fabricated make them an attractive material for a variety of applications including solar cells,² light emitting diodes³ and photodetectors.⁴ However, certain perovskite materials are unstable and undergo degradation when exposed to combinations of moisture, ultraviolet light, oxygen and heat.⁵⁻⁸

There is significant growing interest in the development of perovskite-like materials that self-assemble into low dimensional phases (LDPs) which have modified photonic and electronic properties resulting from exciton confinement effects, with such materials having potential relevance for various device applications. In general, quasi-2D perovskite-like materials adopt a planar or layered structure, and can be formed by partially or completely substituting smaller cations (such as MA, Cs or formamindium, $\text{FA} = \text{CH}(\text{NH}_2)_2^+$) with larger organic cations such as butylammonium ($\text{BA} = \text{C}_4\text{H}_9\text{NH}_3^+$) and phenethylammonium ($\text{PEA} = \text{C}_8\text{H}_9\text{NH}_3^+$) in the precursor ink.^{9,10} Here, the crystal structure of such materials can be thought of being composed of slices along the (100) or (110) plane of a '3D' parent APbX_3 structure (such as MAPbI_3) with larger cations acting as spacer layers that split the lattice along one axis, with octahedral layers terminated by additional halides.¹¹ One such material family is the Ruddlesden-Popper phase (RPP) that is described by the general formula $\text{A}_2\text{B}_{n-1}\text{Pb}_n\text{X}_{3n+1}$, in which A and B are larger and smaller cations respectively.⁹ It has been shown that these RPPs can form natural quantum wells, with cations acting as an electrically insulating barrier layer,¹² permitting the formation of stable excitons.¹³ Importantly, RPPs can have improved moisture tolerance and stability compared to conventional ABX_3 perovskites; a property attributed to organic cations forming a hydrophobic spacer layer.¹⁰ Using this

1 approach, pioneering work by Grancini *et al.* and others has incorporated '2D' layers into perovskite films,
2 creating solar cells that retain efficient performance after one year of operation.¹⁴⁻¹⁶

3 Another class of organic-inorganic hybrid materials that have recently been synthesised are
4 Dion-Jacobson phases (DJPs) which can be described by the general formula $AB_{n-1}Pb_nX_{3n+1}$. These materials
5 form a class of quasi-2D phases that can also be thought of as being composed of a (100) slice taken from a
6 perovskite crystal.¹⁷ However, in contrast to a RPP in which there are two cations per unit cell located in
7 the insulating barrier region, there is only a single organic spacer cation molecule (A) in a DJP that
8 separates the octahedral layers.¹⁸ For this reason DJPs generally have lower bandgaps for a given n-value
9 than their RPP equivalent. For completeness, we note that other lower dimensional perovskite-like
0 materials can also exist, such as 0D and 1D crystals that generally have larger bandgaps compared to their
1 2D and 3D counterparts.^{19,20}

2 In this paper, we investigate the photophysics of mixed quasi-2D and perovskite films formed by
3 adding an excess of MAI into a $MAPb_{3-x}Cl_x$ perovskite precursor blend, and show that the resultant mixed-
4 phase film contains some fraction of LDP. A previous report by Song *et al.* indicates the formation of a
5 variety of LDP structures and other phases in non-stoichiometric MAI:PbI₂ blends,²¹ and others have shown
6 a small MAI excess (1.05:1 MAI:PbI₂) benefits device performance after exposure to moisture.²² However,
7 LDP structures produced via excess organic in the MAI:PbCl₂ 3:1 processing route have not yet been
8 investigated, nor has a structural and photo-physical analysis of such mixed perovskite-LDPs systems been
9 made, despite their observation in literature.²³ In a regular MAPbI₃ perovskite the MA molecule normally
0 occupies the A-site within the ABX₃ perovskite crystal structure (tetragonal space group *I4/mcm* or *I4cm* at
1 room temperature). Here we show that by using excess organic halide material (up to 1/3rd above a
2 stoichiometric 3:1 mixture) this solution stoichiometry and processing route can induce the formation of a

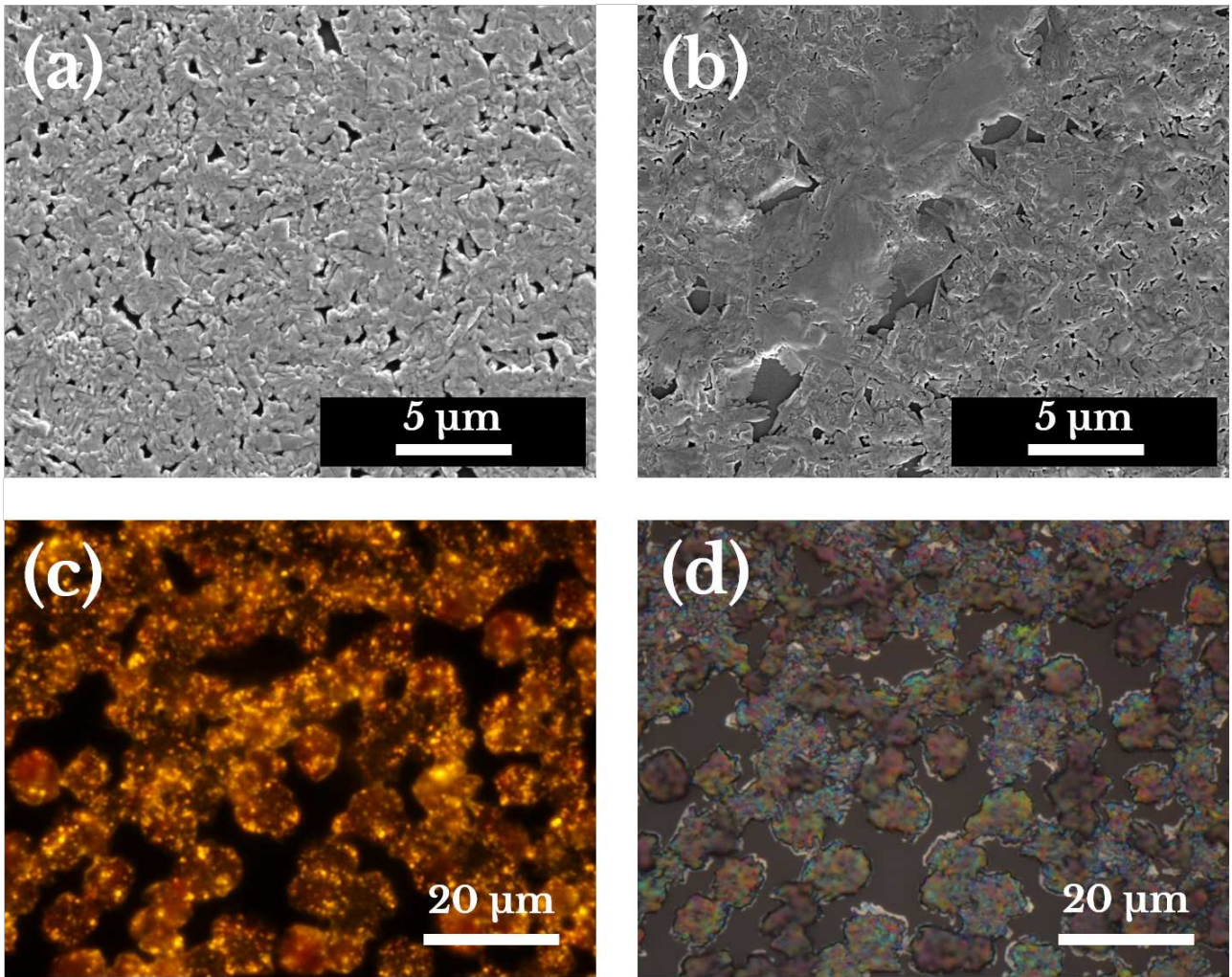
1 structure of layered lead-halide octahedra. We also show that the addition of hydroiodic acid (HI) can
2 induce the formation of crystallographically comparable LDPs in the film and investigate the potential for
3 introduction of dimethylammonium ($\text{DMA} = (\text{CH}_3)_2\text{NH}_3^+$) cations during film preparation as a cause. The
4 formation of low dimensional structures is unexpected, as the MA organic cation used here is relatively
5 small compared to longer chain cations typically observed to form RPPs.²⁴ We propose that the dominant
6 LDP in our material may occupy a similar structure to that of a previously reported DJP/RPP-like phase,
7 with excess MAI or HI in the solution facilitating the formation of isolated octahedral layers in a metastable
8 phase, with the organic spacer layer composition unclear.¹⁸

9 To characterise the structural and optoelectronic properties of this LDP material system, we have
0 used temperature-dependant steady-state and time-resolved photoluminescence (PL) emission (SSPL and
1 TRPL) spectroscopy, along with photoluminescence excitation (PLE), optical absorption and grazing
2 incidence wide-angle X-ray-scattering (GIWAXS). Our GIWAXS measurements indicate that hot-casting such
3 precursor inks in a N_2 atmosphere creates films that are preferentially oriented in the out-of-plane
4 direction, as has been observed with other RPPs.¹⁰ Time-resolved measurements indicate a significant
5 temperature-dependence of LDP fluorescence lifetime, and we conclude that exciton dissociation most
6 likely occurs via thermally activated tunnelling of charge-carriers through the organic spacer at elevated
7 temperatures. We also use PLE to show that excitons can undergo energy transfer between different LDP
8 emissive states. PL mapping shows heterogeneity in film structure over length-scales of around $10\ \mu\text{m}$. Our
9 measurements confirm the complex energy-landscape that is present in films formed from excess MAI or
0 HI precursor inks. Such phase inhomogeneity is also likely to be present in films that are closer to their
1 stoichiometric ratio via this processing route.

2 Results and Discussion

2.1 Thin film topography

Figures 1a and b show SEM images of 3:1 and 3.5:1 (MAI:PbCl₂) films respectively. It can be seen that the films are highly polycrystalline in nature. The structure of the 3:1 film is qualitatively similar to previous measurements on this system, with the 3:1 film characterised by grains with a range of sizes up to ~1 μm.^{25,26} The 3.5:1 film is characterised by comparable structure, in addition to larger semi-crystalline domains with a length scale of 10s of microns, as well as regions with no surface coverage. We emphasize that this study focuses on the structure and photophysics at play in this system, and that the pinholes and reduced film coverage would certainly result in poor performance if this film was used in a solar cell. Figure 1c shows PL emission from a similar 3.5:1 film and a bright-field optical image of the same film is presented in Figure 1d, with both images recorded at room temperature. Here, the bright-field and PL images were taken using an optical microscope, with the PL signal extracted by placing a 600 nm long-pass filter in the collection path.²⁷ These measurements again confirm significant inhomogeneity in the film with non-uniform PL emission from longer wavelengths over the film surface.



1
 2 **Figure 1:** Topographical images of reference (3:1) and excess methylammonium iodide (3.5:1 MAI:PbCl₂) perovskite
 3 samples prepared on quartz. Scanning electron microscope images from a secondary electron (SE) detector of (a) 3:1 and
 4 (b) 3.5:1 films respectively. (c) Fluorescence imaging of a 3.5:1 film excited through a short-pass 550 nm filter and
 5 collected through a 600 nm long-pass filter. (d) Bright-field optical image of the same film area shown in part (c).

6 2.2 X-ray diffraction

7 2.2.1 Experimental data

8 To understand the composition of the crystallites, we characterised their structure using GIWAXS.

9 **Figures 2a** and **b** show typical 2D scattering patterns from 3.5:1 perovskite films annealed in air or in a N₂
 0 filled glovebox respectively. The crystalline planes in the 3.5:1 perovskite film (Figure 2a) annealed in air

1 have some partial orientation; however, there is strong preferential alignment in the same film annealed in
2 glovebox conditions, where we observe a modulation in the azimuthal reflection intensity of the $Q \approx 1.0$
3 \AA^{-1} scattering peak and a number of Bragg spots in the 2D scattering pattern. We note that other studies
4 on RPPs have observed similar orientation effects in films containing the larger cations BA and PEA that
5 were hot-cast.^{9,28,29}

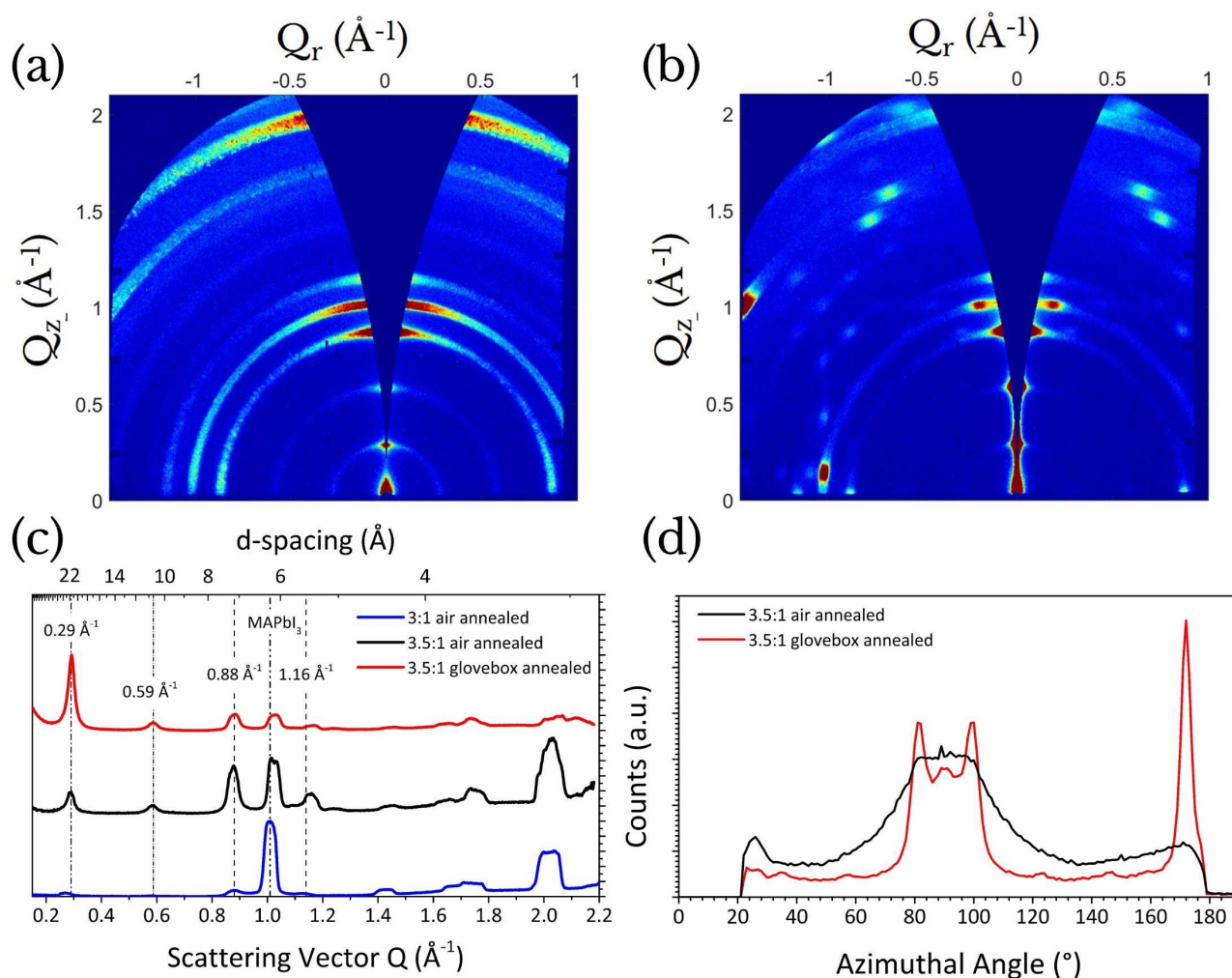
6 Figure 2c shows a radial integration of the GIWAXS pattern from the images shown in Figure 2a and
7 b, together with that of a $\text{MAPbI}_{3-x}\text{Cl}_x$ (3:1) reference film. In all cases, we observe a characteristic
8 reflection at $Q \approx 1.0 \text{\AA}^{-1}$, consistent with the (002)/(110) plane for tetragonal MAPbI_3 perovskite phase or
9 equivalent inter-octahedral spacing, with a small shift to higher Q for the excess organic materials.³⁰⁻³² In
0 films containing an excess of MAI (shown in Figure 2a and b) a series of additional scattering features are
1 detected at $Q \approx 0.29, 0.59, 0.88$ and 1.16\AA^{-1} . Notably the reflection at 0.29\AA^{-1} appears significantly more
2 intense in the glovebox-annealed sample (Figure 2c), and the scattering is anisotropic with numerous Bragg
3 spots in the film annealed under nitrogen in the glovebox. This film has an increased state of order in the
4 out-of-plane direction (Q_z), with some larger Q peaks oriented in-plane (Q_{xy}). We discuss the origin of these
5 features below, but firstly we note that the observation of a characteristic reflection at $Q \approx 1.0 \text{\AA}^{-1}$ suggests
6 the presence of some MAPbI_3 phase in the non-stoichiometric films, or comparably sized Pb-I scattering
7 planes. Orientation of this feature is shown in Figure 2d, where an azimuthal integration of the $Q \approx 1.0 \text{\AA}^{-1}$
8 scattering feature shows both in-plane and out-of-plane orientation for both samples; these observations
9 suggest a preferentially oriented system in the glove-box annealed film. Evidence for the presence of a
0 perovskite phase is strengthened by optical absorption measurements (see later) that also confirm
1 characteristic emission from MAPbI_3 perovskite. However, this characteristic reflection is also evident in

1 other 2D systems,^[18] and a shift to larger Q for the excess organic films is observed ($Q \sim 1.02 \text{ \AA}^{-1}$); a result
2 consistent with a compression of the perovskite lattice.

3 In the stoichiometric sample discussed above (and throughout this study), we have used 1%
4 volumetric addition of hydroiodic acid (HI) to the precursor. This has been found to aid solubility and
5 improve film morphology prepared via this processing route,³³ and has also been used for optimised
6 morphology control of perovskite layers.³⁴ Important work by Ke *et al.* has identified that HI addition to
7 CsPbI₃ perovskite precursor inks using DMF as a solvent leads to the spontaneous formation of DMA which
8 can incorporate into the deposited perovskite film resulting in a mixed cation phase.³⁵ Acids like HI and
9 formic acid (HCOOH) have been shown to shift the reversible reaction of DMF hydrolysis to HCOOH and
0 DMA.^{36,37} Recent work has also shown that films produced via a similar 3:1 lead acetate and MAI
1 conversion route leads to approximately 10% replacement of MA cations in perovskite films by DMA.³⁸
2 These results have implications for this work, and in the 3:1 case low intensity peaks are resolved at $Q =$
3 $0.29, 0.88$ and 1.16 \AA^{-1} (Figure 2d).

4 This led us to investigate whether HI, and perhaps DMA, may assist in the formation of this phase
5 or phases. **Figure S1a** shows XRD of 3:1 MAI:PbCl₂ films with volumetric addition of HI (1-4%), clearly
6 showing the emergence of the same scattering features as in the excess MAI case. To verify this finding, in
7 Figure S1b and c we also compare GIWAXS of a 3.5:1 excess MAI film and a 3:1 + 5 vol% HI film. In both the
8 excess HI and excess MAI case, similar Bragg spots are apparent in the 2D pattern and the scattering is
9 highly comparable. To confirm whether DMA is present in films prepared using excess HI, we undertook
0 solution state ¹H and ¹³C nuclear magnetic resonance (NMR) measurements on 3:1, 3.5:1, 4:1 and 3:1 +
1 5vol% HI films which were then re-dissolved in DMSO-d₆. Somewhat surprisingly, we did not find any peaks
2 that are characteristic of DMA in the ¹H NMR spectra for any composition, with only one carbon-

1 containing species being identified in the ^{13}C NMR spectra (Figure S2). We confirmed the peaks are likely
 2 attributable to MAI by utilising a capillary insert containing dissolved MAI inside the NMR tube for a 3:1
 3 sample (to avoid any chemical interaction) and found good correspondence, suggesting MAI is the only 1H
 4 and ^{13}C containing species in the dissolved films. This observation suggests that the addition of excess HI
 5 to this solution system results in a film containing excess MAI; the mechanism for such a reaction in the
 6 precursor ink is presently unclear.



7

8 **Figure 2:** Grazing incidence wide-angle X-ray scattering (GIWAXS) patterns of (a) 3.5:1 air annealed and (b) 3.5:1 glovebox
 9 (GB) annealed excess organic perovskite films. The x and y axis are the scattering vectors in the xy (Q_{xy}) and in z (Q_z)
 0 planes respectively. (c) Radially integrated GIWAXS profiles (normalised) through all azimuthal angles of stoichiometric 3:1

1 + 1 vol% HI (blue line), 3.5:1 – air annealed (black line) and 3.5:1 – glovebox annealed (red line). (d) Azimuthal integrations
2 around $Q = 1.0 \text{ \AA}^{-1}$ for 3.5:1 annealed in air (black) and in the GB (red) with Q_z perpendicular to the beam path marked.

3 2.2.2 Phase analysis

4 To investigate potential phases induced by excess MAI or HI that may cause additional scattering
5 features, we considered various simulated and experimental data. Previous work has shown that due to
6 the hygroscopic nature of amine salts, monohydrate and dihydrate perovskites can form in similar
7 materials when exposed to high humidity levels ($> 40 \text{ \%RH}$)^{39–42}. Such materials can form 1D and 0D
8 structures respectively,^{40,43–46} with the (100) plane of monohydrate $\text{MAPbI}_3 \cdot \text{H}_2\text{O}$ expected at 0.61 \AA^{-1} ⁴²
9 which is close to our experimentally observed peak at 0.59 \AA^{-1} . Comparison of air-annealed and GB-
0 annealed 3.5:1 films can give useful insight on whether the observed scattering planes at $Q < 1.0 \text{ \AA}^{-1}$ result
1 from the presence of moisture during thermal annealing. However, we find that 3.5:1 films annealed under
2 a nitrogen atmosphere and encapsulated with PMMA are characterised by scattering at the same Q as in
3 the air-annealed sample, confirming hydrate phases are not present (Figure 2c).

4 We note previous simulations of MA_2PbI_4 indicate a unit cell geometry with a (100) plane having a
5 spacing of 19.5 \AA ($Q \approx 0.32 \text{ \AA}^{-1}$), however this plane is not expected to strongly reflect in the $Pnm21$ space
6 group.⁴⁷ Indeed, 1D perovskite-like structures, such as $(\text{MA})_2(\text{DMF})\text{PbI}_5$, have been reported when an
7 excess of MAI is used in an MAI:PbI₂ precursor solution⁴⁸ forming a DMF-complex with coordinating lead-
8 iodide octahedra. However, the same study found that thermal annealing at $70 \text{ }^\circ\text{C}$ was sufficient to remove
9 such DMF phases from the films. It is apparent that the scattering pattern and peaks identified in this
0 material system do not correlate with those of the mixed-halide precursor phase that forms during the
1 early stages of annealing a 3:1 MAI:PbCl₂ precursor (peaks identified by Barrows *et al.* at $Q \approx 0.45, 0.83,$
2 0.88 \AA^{-1} and Stone *et al.* at $Q \approx 0.85, 0.9, 1.1 \text{ \AA}^{-1}$).^{49,50} This phase is observed up to ~ 45 minutes into
3 annealing and is expected to contain a mixture of iodide and chloride. To investigate this, we performed

1 EDX analysis on 3:1 and 3.5:1 samples annealed in air (see **Table S1**) which show a negligible concentration
2 of chloride present after 90 minutes of thermal annealing; a result that further confirms we are not
3 observing this previously reported phase.⁵⁰

4 We propose that the LDP identified here contains lead-halide octahedral planes with a
5 characteristic d-spacing of 21.7 Å, and the addition of MAI to the precursor promotes the formation of LDP
6 structures causing the reflection at $Q \approx 0.29 \text{ \AA}^{-1}$. The peak at 0.59 \AA^{-1} is thus consistent with a second order
7 reflection from the same structure with the peaks at 0.88 \AA^{-1} and 1.16 \AA^{-1} indicative of third and fourth
8 order reflections (see **Table S2** for complete peak analysis). Previous work on this processing route has
9 identified the peaks at 0.88 \AA^{-1} and 1.16 \AA^{-1} that we observe here using non-stoichiometric precursor inks,
0 with the origin of these peaks as yet unexplained.²³ The peak at 0.88 \AA^{-1} also closely matches a reflection
1 produced by the PbI_2 2H polytype, expected at $Q \approx 0.90 \text{ \AA}^{-1}$, and this phase may be present in our film.⁵¹ It
2 is also possible that the 1.16 \AA^{-1} reflection may overlap with that of the (100) plane of MAPbCl_3 (**Table**
3 **S1**).²³ However, EDX measurements show no trace of chloride was detected in either sample, suggesting
4 complete MACl sublimation during film formation and we conclude that the 1.16 \AA^{-1} reflection is entirely
5 related to LDPs.

6 After excluding other phase possibilities present in our material, we now compare our findings with
7 recent work by Soe *et al.* to understand the nature of the LDP.¹⁸ Here a family of DJP/RPP-like materials
8 were synthesised and termed 'alternating cations in the interlayer space' (ACI) perovskites.¹⁸ Structurally,
9 the ACI perovskite exhibits a type II DJP structure⁵² with a lateral offset between adjacent octahedral
0 layers in the a -plane (**Figure S3**) but not in the b -plane (semi-eclipsed configuration), as opposed to an RPP
1 which would be offset in both the a - and b -planes (staggered configuration). In this case, the reported
2 phases were based on mixtures of guanidinium $(\text{C}(\text{NH}_2)_3^+$ or GA) and MA which formed the material family

1 GA(MA)_nPb_nI_{3n+1}. Here, the lattice parameters for GA(MA)₃Pb₃I₁₀ single crystals were determined as a =
2 6.35 Å, b = 12.44 Å and c = 43.97 Å in an orthorhombic centrosymmetric *Imma* space group.¹⁸ In Figure
3 S2a, we compare simulated powder XRD patterns⁵³ from the crystallographic information files produced by
4 Soe *et al.* for the n = 3 variant with our radially integrated GIWAXS patterns for a 3.5:1 GB annealed
5 sample. It can be seen that an excellent correlation is observed in reflected peak positions with the
6 simulated data. Indeed, a reflection corresponding to the (002) plane of the GA(MA)₃Pb₃I₁₀ ACI phase is
7 observed at Q ≈ 0.29 Å⁻¹, corresponding to a d-spacing ≈ 22 Å. The (004) and (006) planes are located at Q
8 ≈ 0.57 and 0.86 Å⁻¹, together with stronger reflections from the (101) and (020) planes at Q ≈ 0.99 and 1.01
9 Å⁻¹ (d-spacing = 6.3 and 6.2 Å⁻¹), respectively. We therefore consider an n = 3 type II DJP structure may be
0 a component of the scattering data, similar to the structure reported by Soe *et al.* with a spacer layer
1 resulting from the excess MAI or HI precursor. This significant correlation suggests we have thin-films
2 consisting of multiple phases, including an LDP structure that may be similar in nature to the ACI phase.
3 Although the exact composition of the spacer layer that leads to this multiple quantum well structure is
4 still unclear, our NMR measurements presented in Figure S2 suggest that the only organic component is
5 MA.

6 2.2.3 Modelling

7 The possibility of a perovskite-like phase similar to the reported ACI phase but with MA substituting
8 GA in the interlayer is intriguing. To understand this possible crystal structure, we carried out density
9 functional theory (DFT) calculations using two appropriate DFT functionals: PBEsol⁵⁴ and the van der Waals
0 functional with C09 exchange⁵⁵ (further referred to as C09). PBEsol has commonly been used for modelling
1 lead-iodide perovskites^{19,56-60} and has accurately predicted the lattice parameters of bulk and layered
2 perovskites.⁵⁸⁻⁶⁰ The C09 functional has recently been applied to perovskites⁶¹⁻⁶³ and because this

functional is able to describe weak van der Waals interactions, it is also expected to give a more reliable description of the interactions in the dielectric spacer layers of LDPs compared to the GGA-type PBEsol functional.

In **Figure S4a** we show simulated pXRD patterns taken from the PBEsol and C09 possible $\text{MA}_4\text{Pb}_3\text{I}_{10}$ structures overlaid with radially integrated GIWAXS pattern from a 4:1 sample. Here, there is commonality between the experimental and theoretical scattering patterns, with the C09 functional more closely matching the scattering features. In **Figure S4b** we show significant octahedral distortions in one view of the crystal structure and in **Figure S4c** the modelled translation in the ab-plane is seen (as is noted with the ACI perovskite).^{18,64} This phase would therefore have comparable symmetry to a DJP perovskite but with the stoichiometry of a monocation RPP. The calculated and experimental lattice parameters using both PBEsol and C09 functionals applied to the (previously reported) mixed cation $\text{GAMA}_3\text{Pb}_3\text{I}_{10}$ and all- $\text{MA}_4\text{Pb}_3\text{I}_{10}$ crystal structures are given in **Table S3**. We caution that this analysis is reliant on sets of assumptions driven by GIWAXS data and literature; as such, further analysis using techniques such as Rietveld analysis of powdered or single crystal samples and extended X-ray absorption fine structure should be applied for full structural refinement.^{50,65} Single crystals of this phase may require the use of a complex synthesis process if - as we suspect - there is a sublimation (MAI) and phase conversion process during film formation.

2.2.4 Metastability

Having demonstrated the existence of low-dimensional nanostructures within our films, we also note that such mixed phase films undergo a phase transition following exposure to high humidity, indicating that the quasi-2D layered structure is metastable. Whilst such films are stable under ambient conditions ($\sim 25^\circ\text{C}$ and $\sim 30\% \text{RH}$), exposure to humid air ($>50\% \text{RH}$) causes them to rapidly lose their dark-

1 red colour and convert to a dark-brown film containing MAPbI₃ perovskite and hydrates (see images and
2 GIWAXS patterns in **Figure S5**). We suspect that moisture may facilitate escape of excess MAI from the
3 film, with the layered structure collapsing to more energetically favourable perovskite and hydrate
4 structures, although the precise mechanism is unclear.

5 2.3 Spectroscopy

6 2.3.1 Temperature-dependent absorption and photoluminescence

7 To investigate the co-existence of the LDP and MAPbI₃ phases, we measured steady-state
8 photoluminescence (SSPL) and optical absorption as a function of temperature. **Figure 3a** plots the
9 normalised absorption (red line) and PL emission from a stoichiometric 3:1 perovskite film at 290 K and 12
0 K. The film absorption (at 290K) is relatively featureless and is characterised by a band-edge at 758 nm. The
1 PL emission from this film is dominated by a peak centred at 763 nm which is expected from charge carrier
2 recombination within MAPbI₃³⁰ and red shifts to 772 nm at 12 K with a second, less intense peak at 740
3 nm. Emission from these features becomes weaker as the temperature is reduced, with the low energy-
4 region of the spectrum becoming dominated by an emissive peak centred at 770 nm, corresponding to
5 emission from the orthorhombic phase of MAPbI₃.^{30,66}

6 For the non-stoichiometric case, Figures 3b and c show normalised absorption and PL emission
7 spectra for a 3.5:1 air-annealed perovskite film at 290 K and 12 K respectively. In contrast to the 3:1 film,
8 we observe a more complex absorption spectrum at 290 K characterised by a broad unresolved band at
9 550 nm together with a weak band edge at 760 nm. As the temperature is reduced, both the absorption
0 and emission evolve into the spectra shown in Figure 3c, indicative of a complex energy landscape (the full
1 temperature series of PL emission for the 3.5:1 perovskite is shown in Figure 3d). As the temperature is
2 reduced, the absorption bands between 500 and 590 nm split into distinct peaks at 500, 515, 542, 562 and

1 582 nm, with the lower energy band edge shifting to 750 nm. As shown in **Figure S6**, the low-temperature
2 absorption profile for a stoichiometric (3:1) film is characterised by a single excitonic feature close to the
3 band-edge. Therefore, additional absorption features at low temperature in the 3.5:1 films must result
4 from the introduction of excess MAI into the precursor solution.

5 The PL for the 3.5:1 film is similarly structured, with strong emission peaks observed at 546, 566,
6 586, 606, 641 and 803 nm at 12 K. There is one-to-one correspondence between peaks observed in the
7 emission spectrum at 546, 566 and 586 nm with the peaks observed in absorption at 542, 562 and 582 nm.
8 This observation suggests a series of excitonic states with a Stokes shift of around 4 nm at 4 K. A weaker
9 emission peak was observed sporadically in 3.5:1 samples at 512 nm (see Figure 3c inset, note that the
0 inset spectrum was recorded using a PL mapping system – see later). This 512 nm peak could be due to
1 localised lead iodide formation in the film, with this emissive peak correlating with previous reports.^{67,68}
2 Significantly however, in films in which we might expect the lowest fraction of PbI_2 (i.e. those containing
3 the higher (4:1) organic ratio), we find that the intensity of the 512 nm peak is greatest. This suggests
4 therefore that the peak at 512 nm likely results from LDPs in the film (**Figure S7**). We also find that PL
5 emission intensity is significantly higher from the 4:1 sample with two low intensity peaks also detectable
6 at room temperature (see Figure S7).

7 In the 3.5:1 film (see Figure 3d), it can be seen that the band-edge PL undergoes a small red-shift of
8 27 nm as the film is cooled from 290 K to 185 K, being located at 761 nm and at 788 nm, respectively. This
9 peak then blue shifts to 780 nm at 110 K (a temperature just below the tetragonal to orthorhombic
0 transition in the perovskite phase)⁶⁹ and broadens considerably as the film is cooled to 12 K. We have
1 shown using a hole-quenching ITO/PEDOT:PSS substrate (see **Figure S8**) that this broadening can be

1 suppressed, a result that suggests that this red shift and broadening results from increased recombination
2 via hole trap states at low temperature.⁷⁰

3 Finally, we consider the origin of the intense peak at 641 nm that is broader than the higher energy
4 features, and is apparently composed of several unresolved, narrow peaks. The origin of the feature is not
5 clear, but we speculate that this might result from interface phases or charge transfer states that exist at
6 the boundaries between the LDP and perovskite material. We base this speculation on the observed
7 reduction in intensity of this peak in the glovebox-annealed 3.5:1 film (see **Figure S9**). In the 4:1 precursor
8 blend ratio film, we also observe a suppression in emission both around 640 nm and at longer wavelengths
9 (see Figure S8b and S9), confirming that 4:1 sample is phase-pure with uniquely LDP emission at low
0 temperature. This leads us to interpret the broad emissive peak at 640 nm as coming from interface or
1 charge-transfer states between the LDP and perovskite, with the approximate LDP-specific and perovskite
2 regions annotated in Figure 3d.

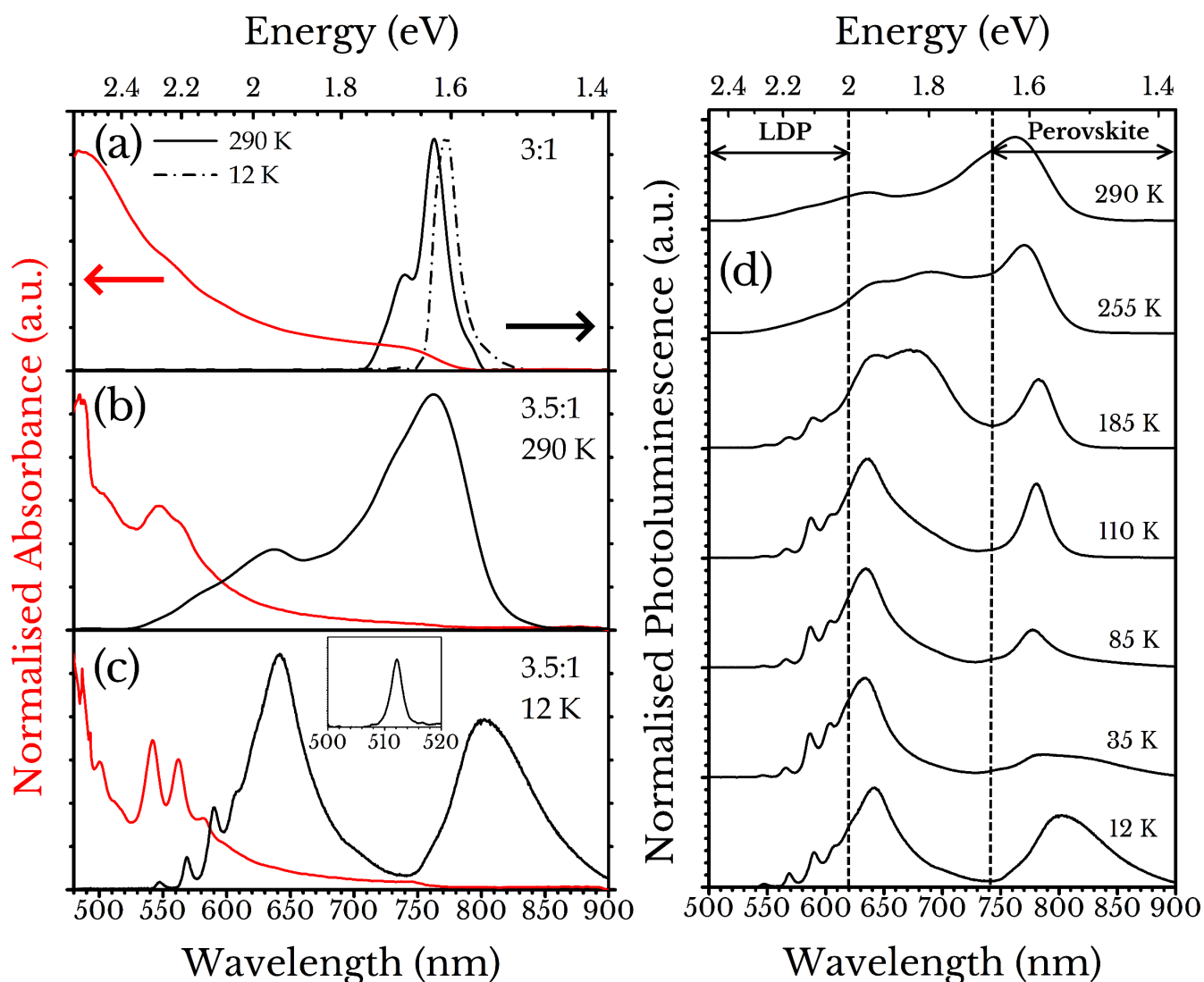


Figure 3: (a) Steady-state photoluminescence (SSPL) at 290 K (black), 12 K (dashed black) and absorption at 290 K (red) of a 3:1 perovskite film. (b,c) Typical SSPL (black) and absorption (red) of 3.5:1 at (b) 290 K and (c) 12 K. (d) Temperature series of SSPL spectra for a 3.5:1 film between 290 K and 12 K showing the emergence of short wavelength LDP emissive states and gradual blue shift of emission from the perovskite phase.

2.3.2 Interpretation of LDP emission

The photoluminescence features at 546, 566 and 586 nm are of particular interest, and in the 4:1 sample represent the dominant emissive species. The absorption profile shown in Figure 3c resembles that of a quasi-2D perovskite film using larger cation spacers.⁷¹⁻⁷³ Through analysis of the complete

1 temperature-dependent absorption spectral-series (see **Figure S10**) we find that the absorption peak
2 observed at 547 nm undergoes a blue-shift of 5 nm as the temperature is reduced from 290 K to 12 K.
3 Similar features have been observed in quasi-2D films at room temperature^{28,74,75} and have been ascribed
4 to excitonic absorption and emission from n -layered quasi-2D crystals.^{19,24,44,76} Specifically, quasi-2D ACI
5 hybrid $\text{GA}(\text{MA})_n\text{Pb}_n\text{I}_{3n+1}$ crystals produce fluorescence at peak emission wavelengths of $\lambda \approx 550, 605$ and
6 645 nm for $n = 1, 2$ and 3 , respectively, and the absorption profiles seen in these ACI perovskites show
7 similar, but broader, multiple excitonic absorption peaks to those seen Figure 3c.¹⁸ Indeed in films
8 produced with the $n = 3$ target composition ($\text{GAMA}_3\text{Pb}_3\text{I}_{10}$), multiple absorbing states have been observed
9 and attributed to different phases in the film; a result also consistent with previous analysis on single
0 crystals.^{18,64} It is possible therefore the absorption peaks observed at shorter wavelengths correspond to
1 different perovskite-like structures having reduced dimensionality.

2 However, other explanations for multiple emissive peaks from a single LDP are possible. Two
3 absorption edges in the pure $n = 1$ RPP material BA_2PbI_4 have been attributed to band edge and excitonic
4 absorption, so individual phases within this mixed phase may have multiple absorbing features.⁷⁷ Whalley
5 *et al.* have recently shown that deformation at the grain boundaries in MAPbI_3 caused by a tilting of the
6 octahedra due to thermal broadening gives rise to a 40 meV shift of the bandgap.⁷⁸ We note that the
7 emission peaks seen at 546 and 566 nm differ in energy by 80 meV, and it is therefore possible that the
8 multiple emissive states could result from disorder at grain boundaries, or by having disconnected
9 octahedra between LDP structures which would reduce tilting constraints.

0 We conclude therefore that the 3.5:1 films are comprised of a perovskite phase (as identified by the
1 band edge absorption and emission at 761 nm) that co-exists with a series of LDP emissive states with
2 absorption and emission between 505 and 605 nm. The strong temperature dependence of PL emission

1 intensity indicates the existence of a thermally activated process that results in the dissociation of excitons
2 localised in LDPs. If excitonic in nature, it is possible that they result from dielectric confinement within
3 different phases consisting of multiple n-dimensional layers of lead-iodide octahedra, leading to different
4 well widths and consequently different exciton binding energies. However, our GIWAXS data suggests this
5 is not the case, with simulated scattering data from only one layered phase correlating well with the
6 experimental data. We might expect that a mixture of LDP and perovskite phases would be dependent on
7 the initial precursor blend ratio, as has been observed in films of RPP phases.⁷⁹ Within the range of
8 stoichiometries explored in this study, we do not observe multiple LDP phases; rather the peaks identified
9 in the scattering pattern from a 4:1 MAI:PbCl₂ ratio precursor blend film (see Figure S2a) are comparable to
0 those from a 3.5:1 sample (see Figure 2). This suggests that the film contains a single LDP phase, and that
1 increasing the MAI ratio simply increases the proportion of material within the film that is in this phase.

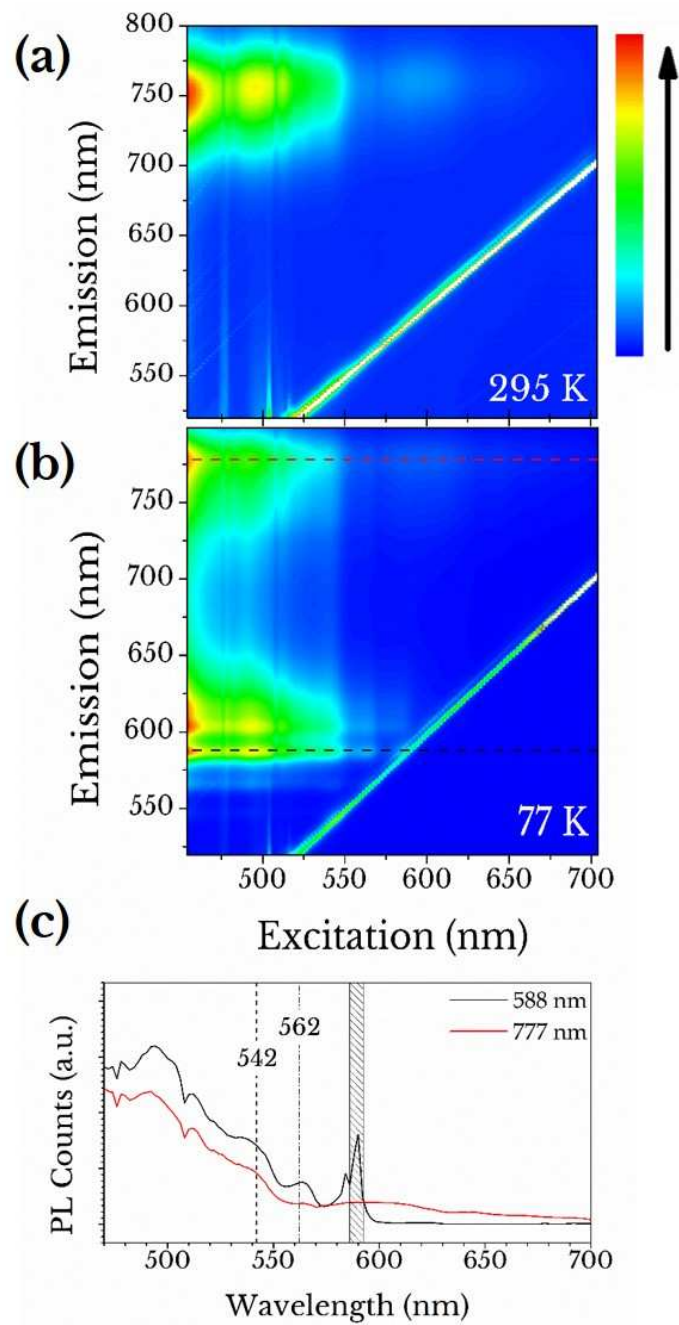
2

3 2.3.3 Photoluminescence excitation spectroscopy

4 To evidence possible energy transfer between the different observed states we investigated their
5 emissive behaviour as a function of excitation wavelength. Two-dimensional PL excitation (PLE) spectra are
6 plotted in **Figure 4a** and b for a non-stoichiometric 3.5:1 sample recorded at temperatures of 295 and 77 K
7 respectively. Here the scatter from the excitation laser appears as a diagonal band across the image (note
8 that the emission spectra are only plotted for wavelengths > 450 nm due to the limited operational range
9 of the spectrometer grating used to detect emission). At both temperatures, the excitation of the sample
0 up to ~550 nm results in strong band-edge perovskite emission around 750 nm.

1 In Figure 4c, we plot a horizontal cross-section through Figure 4b at wavelengths of 588 nm and 777
2 nm (shown using dotted lines), corresponding to a PLE spectrum of one of the LDP emission peaks and

1 emission around the perovskite band-edge respectively. Interestingly, we find that the excitation spectrum
2 of emission at 588 nm indicates excitation resonances at 542 and 562 nm, signifying some degree of
3 energy transfer (most likely by dipole-dipole coupling) between the different LDP emissive states. This has
4 been observed previously in RPP systems with excitonic energy transfer from wider-bandgap, lower n-
5 dimensional regions to narrower-bandgap, higher n-dimensional regions and also to perovskite phases in a
6 cascade-like manner.⁸⁰ In this system, such resonance features are relatively weak compared to the PLE of
7 the bulk emission, with the PLE spectrum at 777 nm being comparatively featureless. This observation
8 indicates that direct energy transfer between the LDP states and the co-existing bulk perovskite phase is a
9 relatively inefficient process. Significantly, the PLE signal recorded over the excitation range 600-700 nm is
0 relatively greater when detecting at 777 nm (corresponding to emission from the bulk perovskite phase).
1 This reinforces our hypothesis that the spectral region 600-700 nm largely corresponds to charge-transfer
2 or interface states between LDP and perovskite phases.



1

2 **Figure 4:** Photoluminescence excitation (PLE) contour plots shown for a 3.5:1 sample glovebox annealed sample on quartz
 3 at (a) 295 K and (b) 77 K. (c) Horizontal slices of the plot in (b) at given emission wavelengths 588 nm (black) and 777 nm
 4 (red). The shaded section indicates scattered signal from the excitation laser around 588 nm.

2.3.4 Time-resolved photoluminescence

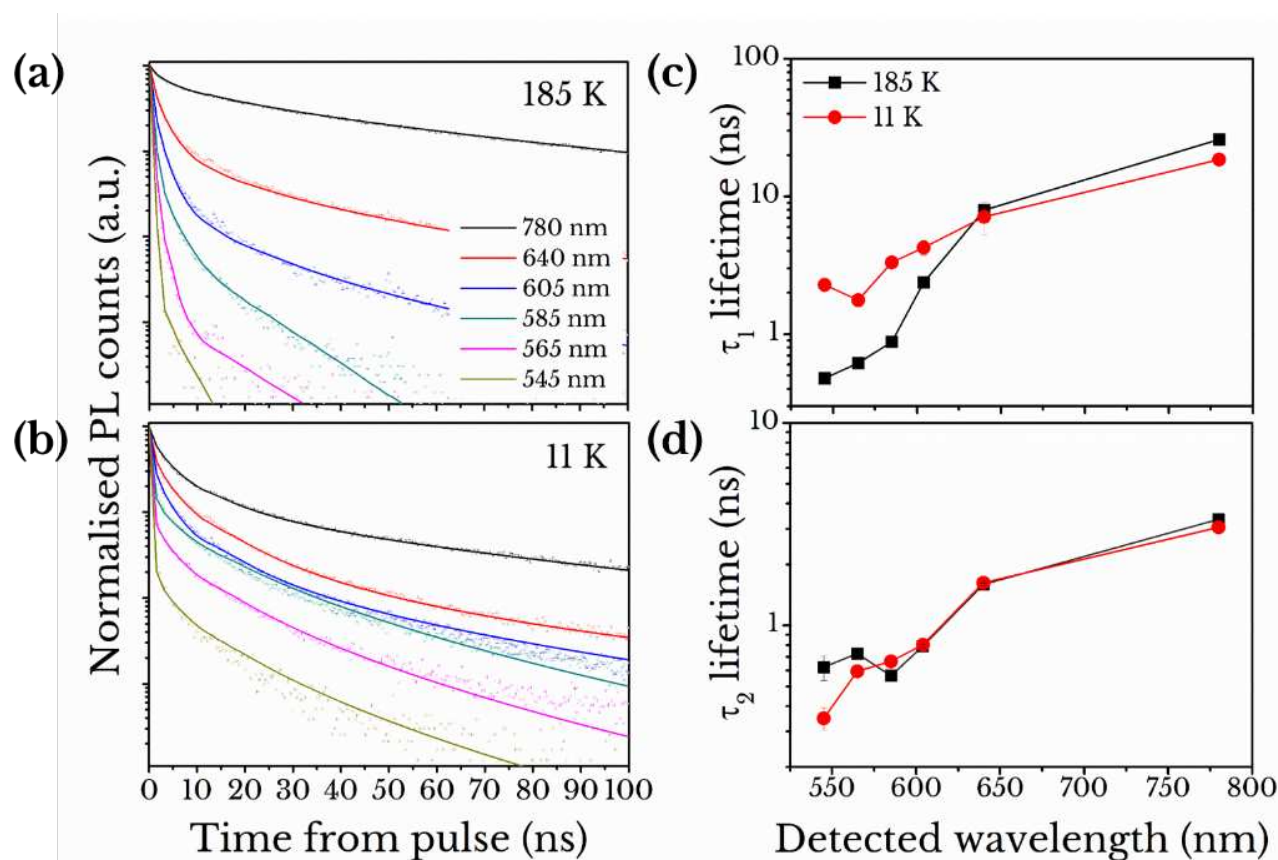
To further understand the photophysics of such LDP states, we measured time-resolved luminescence of a 3.5:1 air-annealed film as a function of wavelength at a temperature of 12 K and 185 K.

Figure 5a and **b** show the (normalised) PL decay lifetimes corresponding to the emissive peaks observed at 546, 566, 586, 646, and 770 nm. To quantify the transient behaviour, these were fitted to double stretched exponentials of the form $I = Ae^{-(t/\tau_1)^{\beta_1}} + Be^{-(t/\tau_2)^{\beta_2}}$, with such biexponential transients commonly used to describe relaxation in disordered systems and thus model PL decay in perovskite materials. Indeed, multi-exponential decay is associated with discrete populations of states undergoing relaxation through independent decay channels.

We plot the PL decay lifetime of the fast and slow PL decay transients in **Figure 5c** and **d**. It can be seen that decay lifetimes increase as a function of detection wavelength; an observation consistent with the increase in PL intensity from the LDP states as a function of increasing wavelength (see **Figure 3c, d**). The general increase in decay lifetime as a function of emission wavelength observed for both short and fast transients is consistent with an energy cascade process from higher energy LDPs to lower energy states, as suggested by PLE spectroscopy (see **Figure 4c**). However this effect may also result from low temperature confinement effects of excitons in LDPs of different size which modify radiative rates.^{81,82}

It is noticeable that the t_1 (slow transient) emission lifetime of the localised LDP states (detected at wavelengths < 620 nm) increases as the temperature is reduced (see **Figure 4c**). In a perovskite phase, this recombination process would likely be dominated by bimolecular recombination, with this rate typically increasing at low temperature as a result of enhanced carrier mobility.⁸³ In the perovskite phase (emission at 770 nm) we see this behaviour, and observe a slight decrease in the t_1 lifetime at low temperature. The reverse is instead observed for the LDP states - an observation consistent with enhanced localisation of

1 excitons at low temperature. Notably at temperatures > 200 K such states appear to dissociate rapidly. We
 2 ascribe this dissociation process to either the electron or hole undergoing thermally assisted tunnelling
 3 into regions of perovskite.



4
 5 **Figure 5:** Time resolved photoluminescence spectroscopy for 3.5:1 film air annealed on quartz at (a) 185 K and (b) 12 K
 6 shown with fitting (solid lines). The coloured lines represent isolated wavelengths of 780 nm (black), 640 nm (red), 605 nm
 7 (blue), 585 nm (cyan), 565 nm (magenta) and 545 nm (gold). (c) First (τ_1) and (d) second (τ_2) time constant parameters of
 8 double stretched exponential fits to the decay transients for the emissive peaks plotted against their emission wavelength.

0 2.3.5 Photoluminescence mapping

1 Clearly, the observation of energy transfer between LDP states and charge-carrier tunnelling from
 2 LDP states into the perovskite phase suggests that such phases must be intimately mixed at length-scales

1 corresponding to exciton/carrier diffusion-lengths. To confirm the length-scales of this mixing, we used PL
2 mapping performed at 4 K to characterise the distribution of emission from the various emissive states
3 from a 3.5:1 film. This is shown in **Figure 6** where we plot the integrated-distribution of luminescence
4 centred at 512 nm (PbI₂ or LDP emission), 546 nm and 566 nm (LDP emission) and 760 nm (perovskite). The
5 emission spectrum was integrated around the centre wavelengths with limits $\lambda \pm 5$ nm. As was evident in
6 the optical microscopy images shown in Figures 1c and d, we see a series of domains whose lateral size is
7 of the order of 10 μ m, indicating regions of emissive material. The distribution of the emission from the
8 LDPs and the perovskite is similar but there is some variation in distribution of emission from these
9 different phases, partially from self-absorption resulting from thickness fluctuations of the film. The
0 similarity in particular between the 546 and 566 nm images suggests that this LDP emission is from one
1 LDP phase with multiple emissive peaks rather than multiple phases. The significant self-similarity between
2 LDP and perovskite emission suggests that these phases are mixed at a length-scale finer than the spatial
3 resolution of our PL mapping setup (around 1.3 μ m).

4

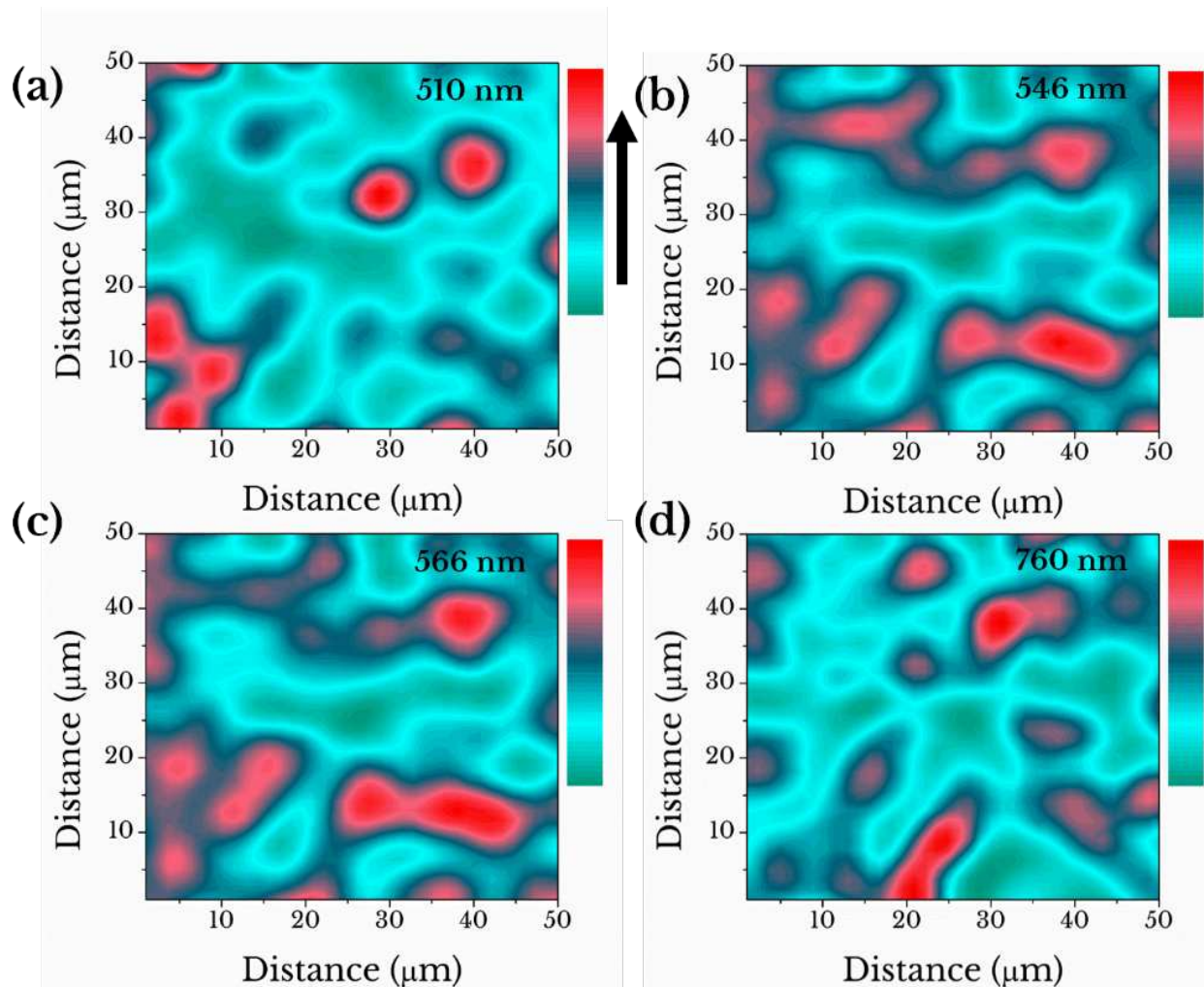


Figure 6: Contour plots of the emission from LDP and bulk perovskite states integrated around (a) 510 nm (LDP or PbI_2), (b) 546 nm (LDP), (c) 566 nm (LDP) and (d) 760 nm (MAPbI_3). The z-axis here is the integrated total PL intensity under the spectrum with limits ± 5 nm around the centre wavelength. Each plot has individual z-axis limits between its maximum and minimum value and are not individually normalised. Regions of very low intensity are without any material.

3 Conclusion

In summary, we have explored the structure and photophysics of perovskites from mixed-halide precursor inks containing a non-stoichiometric excess of methylammonium iodide (MAI). We show using optical and scanning electron microscopy that the thin-films created are highly polycrystalline. Grazing incidence X-ray scattering reveals the presence of new scattering features at $Q = 0.29, 0.59, 0.88$ and 1.16

1 \AA^{-1} that co-exist with the bulk perovskite phase. This suggests strong reflections from lead iodide
2 octahedral layers spaced by 21.7\AA , with such spacing assisted in some way by the excess organic (MAI or
3 HI) solution stoichiometry. We have performed a detailed analysis of such scattering patterns, and
4 compare this to simulated powder-XRD from the previously reported $\text{GA}(\text{MA})_n\text{Pb}_n\text{I}_{3n+1}$ material family. In
5 particular, we find a close correspondence to the $n = 3$ variant. Based on this we tentatively suggest that
6 our film may include a Dion–Jacobson / Ruddlesden-Popper phase $\text{MA}_4\text{Pb}_3\text{I}_{10}$ which shows comparable
7 scattering features after modelling using two DFT functionals. When off-stoichiometric films are annealed
8 in a glovebox under low-moisture conditions, the crystalline phase-purity improves, with a highly oriented
9 film formed. Optical spectroscopy performed on films as a function of temperature reveals the presence of
0 excitonic-like features in both emission and absorption at temperatures $< 200 \text{ K}$, and at higher organic
1 ratios interface or charge-transfer state emission between the LDP and perovskite is suppressed, and the
2 possibility of multiple emissive states either from one phase or different LDPs is explored. Using
3 photoluminescence excitation spectroscopy we show some degree of energy transfer between low-
4 dimensional states with different energies, suggesting close intermixing. Time-resolved PL emission
5 measurements demonstrate that the emissive states have reduced lifetimes at elevated temperature,
6 however this reduced lifetime most likely results from exciton dissociation caused by thermally assisted
7 tunnelling of charge-carriers into regions of perovskite. Photoluminescence mapping of the emission from
8 perovskite and LDPs performed with a spatial resolution of $\sim 1.3 \mu\text{m}$ further confirms a mixed-phase film of
9 the order of exciton and charge-carrier diffusion lengths; a result consistent with energy transfer in a
0 cascade-like structure from higher energy to lower energy states. Strong co-localisation of the short
1 wavelength LDP emission indicates multiple emissive states resulting from one phase. Our measurements
2 indicate a significant degree of energetic inhomogeneity in a perovskite film in which the organic cation is
3 in excess. This work highlights the potential phase behaviour that can occur with off-stoichiometric (excess

MAI or HI) processing, leading to the generation of low-dimensional nanostructures containing additional MA cations. It is likely that such structures and the interface between the LDPs and the perovskite are associated with charge-trapping states that result in significant recombination pathways.

4 Experimental

Materials preparation: To fabricate the LDP containing films, precursor compounds were mixed in anhydrous dimethylformamide (DMF) at molar mixing ratios of MAI:PbCl₂ (for convenience we refer to samples by their MAI:PbCl₂ molar precursor ratio) and emphasise that this is not the stoichiometry of the resultant film. Unless otherwise stated, hydroiodic acid (HI) was added to the precursor at 1 vol%, which we have found to improve lead chloride solubility as well as increasing film coverage and homogeneity.^{33,84} Films using a 3:1 (stoichiometric) molar ratio form the well-documented perovskite material MAPbI_{3-x}Cl_x,⁸⁵ and we routinely use this material system in an ‘inverted architecture’ device format to create solar cells having a power conversion efficiency of up to 14%.³³ Films were deposited onto quartz substrates that had been cleaned by sonication sequentially for 10 minutes in hot 2% Hellmanex solution, 10 minutes in boiling deionised water and finally 10 minutes in isopropyl alcohol. After drying with nitrogen, substrates were UV ozone cleaned for 15 minutes. To deposit the perovskite film, the precursor ink was heated to 70°C, and then spin-cast onto the quartz glass at 90°C. After spin-coating, films were annealed in air or under nitrogen at 90°C for 90 minutes and then encapsulated using a ~200 nm thin film of poly(methyl methacrylate) (PMMA) spin-coated onto their surface from a toluene solution. We have found that without encapsulation, such non-stoichiometric perovskites rapidly convert to different phases on contact with moist air; with only small excess a more textured MAPbI_{3-x}Cl_x material is formed.²²

1 **X-ray diffraction:** GIWAXS was performed using a Xenocs Xeuss 2.0 system with 9.2 keV X-rays produced
2 using a liquid Gallium MetalJet (Excillum) source. X-rays were then directed onto the perovskite thin-film of
3 interest with all films being held under vacuum to reduce unwanted scatter. The X-rays scattered from the
4 film were then detected using a Pilatus3R 1M detector at approximately 300 mm sample to detector
5 distance. GIWAXS data was corrected and reshaped using the GIXSGUI MATLAB toolbox.⁸⁶ X-ray
6 diffractograms (Figure S1a) were collected using a PANalytical X'Pert Pro diffractometer in Bragg-Brentano
7 geometry.

8 **Scanning electron microscopy:** An FEI Inspect F microscope was used in secondary electron mode to
9 image the surfaces of perovskite films. Samples were prepared with layers glass/ITO/PEDOT:PSS and
0 perovskite at the stated compositions. The beam had an accelerating voltage of 5 kV and spot size 3 mm at
1 a working distance of 11 mm. Images were captured rapidly on unexposed areas of the film to avoid any
2 degradation due to the beam energy (the observed large grains were found to change their appearance
3 and fracture after prolonged exposure).

4 **Absorption measurements:** Absorption spectra were determined through the change in transmission of
5 light from a deuterium/tungsten-halogen lamp that was imaged through the sample, with light again being
6 detected using a fibre-coupled Ocean Optics CCD-detector. For all measurements, the samples were placed
7 in an Oxford Instruments Drystat, with temperature being controlled between room temperature and 4K.

8 **Photoluminescence:** Steady-state photoluminescence was recorded using a fibre-coupled BETEK BTC112E
9 CCD array spectrometer at an excitation wavelength of 405 nm with samples positioned within an APD
0 Cryogenics DMX helium cryostat. The time-dynamics of the PL decay were recorded using a time-
1 correlated single photon counting (TCSPC) technique. Here, samples were placed in an APD Cryogenics
2 DMX helium cryostat, with 405 nm laser pulses (having width of 140 fs at a repetition rate of 4 MHz and

1 fluence of 3.8 nJcm^{-2}) provided by a Coherent Chameleon Ultra Ti-Sapphire laser system used to excite the
2 film. The emitted PL was first monochromated using a Bentham M300 single monochromator and then
3 detected using a single photon counter APD detector. We estimate the temporal resolution of TCSPC
4 system to be $\approx 300 \text{ ps}$.

5 **Photoluminescence excitation (PLE):** To investigate energy-transfer processes within the films PL emission
6 intensity was measured over the spectral-range 520-800 nm while the excitation wavelength was scanned
7 between 455 and 705 nm in 2 nm increments. Here, the excitation was provided by light from a Fiannium
8 supercontinuum laser that was filtered using a SPEX monochromator (FWHM = 1.5 nm). Emission was then
9 recorded using an Andor 303i CCD spectrometer, with samples being mounted in a cold-finger nitrogen
0 cryostat.

1 **Photoluminescence imaging:** The bright-field image was recorded using a commercial bright-field optical
2 microscope (LV150N, Nikon). The related PL image was recorded using the same microscope, with a 550nm
3 short-pass filter placed in the excitation path. The PL signal was then extracted by placing a 600 nm long-
4 pass filter in the collection path.²⁷

5 **Photoluminescence mapping:** To understand the length-scales over which electronic inhomogeneity
6 occurs within such films, we have used a microscopic PL mapping technique performed both at room
7 temperature and liquid helium temperatures. Here, the perovskite cast on quartz was placed on an (x,y)
8 translation stage and held under vacuum in a cryostat. A 405 nm laser was then focused onto a $<2 \mu\text{m}$
9 diameter spot on the sample surface through an infinity corrected objective (EO 20x NA = 0.6), with the
0 PL emission at each point collected using the same objective and directed through a 500 nm long-
1 pass filter to a 0.75m spectrometer and a high-sensitivity, liquid nitrogen cooled charge-coupled device to
2 collect the emitted photons. The laser spot was then scanned across the sample surface in steps of 1.25

1 μm . At each location the PL emission spectra was integrated with limits ± 5 nm around a central emission
2 wavelength to allow us to map out the relative spatial distribution of the different LDP states and the
3 perovskite band-edge emission.

4 **NMR spectroscopy:** Perovskite and excess organic LDP samples were prepared on glass in accordance with
5 the above methods. Films were dissolved in DMSO- d_6 by running the deuterated solvent repeatedly over
6 the sample surface into a large vial. Around 10 films were used for each sample type to maximize the
7 analyte content. NMR spectra were recorded using a Bruker AVANCE III 400 spectrometer. ^1H spectra
8 were recorded at 400.2 MHz, using a 30 degree pulse and a relaxation delay of 10s to ensure full
9 relaxation. 16 transients were recorded using a spectral window of 8.2 kHz with 64k acquisition points. ^{13}C
0 spectra were recorded at 100.6 MHz, using the "UDEFT" sequence⁸⁷ to ensure a more quantitative
1 response across both protonated and non-protonated C^{13} environments. This data was recorded using
2 1600 transients, a 23.8kHz acquisition window and 21k acquisition points.

3 **Computational methods:** Density functional theory (DFT) calculations were carried out using the SIESTA
4 code (version 4.0).^{88,89} Double-zeta polarised (DZP) finite-size numerical atomic orbitals were used in
5 combination with Troullier-Martins norm-conserving pseudopotentials. The basis set and relativistic
6 pseudopotential for Pb were downloaded from the SIESTA online basis sets database.⁹⁰ For C, N, H and I,
7 basis set size was controlled using the energy shift (i.e. the energy cost of confining the atomic orbital to a
8 finite-range) of 10 meV, and the non-relativistic pseudopotentials were downloaded from the SIESTA
9 online pseudopotentials database.⁹⁰ The Brillouin zone was sampled using the `kgrid_cutoff` parameter of
0 30 Å, resulting in 75 **k**-points. Two DFT functionals were used: the PBEsol functional⁵⁴ which is based on the
1 generalized gradient approximation (GGA), and the van der Waals functional with C09 exchange.⁵⁵ PBEsol
2 has been widely used for modelling lead-iodide perovskites^{19,56–60} and has been shown to be accurate in

1 predicting the lattice parameters of bulk and layered perovskites.⁵⁸⁻⁶⁰ The C09 functional has recently been
2 applied to perovskites⁶¹⁻⁶³ and our tests show that it is accurate in predicting the lattice parameter of bulk
3 methylammonium lead iodide. Lattice optimization of cubic MAPbI₃ using the computational settings
4 described above without any symmetry constraints gives the values $a = 6.32 \text{ \AA}$, $b = 6.27 \text{ \AA}$, $c = 6.40 \text{ \AA}$, in
5 good agreement with the experimental value $a = 6.32 \text{ \AA}$.⁵⁸ All atom positions and lattice parameters were
6 fully optimised without applying any symmetry constraints, with the displacement threshold of 0.1 \AA and
7 the force of 0.04 eV \AA^{-1} .

8 5 Acknowledgements

9 This work was funded by the UK Engineering and Physical Sciences Research Council (EPSRC) via grants
0 EP/M025020/1 'High resolution mapping of performance and degradation mechanisms in printable
1 photovoltaic devices' and EP/M014797/1 'Improved Understanding, Development and Optimization of
2 Perovskite-based Solar Cells'. We also thank the EPSRC for PhD studentships via the University of Sheffield
3 DTG account (R.K.) and from the Centre for Doctoral Training in New and Sustainable PV, EP/L01551X/1
4 (B.F., G.P., and J.S.). LS and AIT were supported by the European Union's Horizon 2020 Marie Skłodowska-
5 Curie ITN Spin-NANO under grant agreement 676108. We further thank Alan Dunbar and EPSRC grant
6 EP/K001329/1 which funded the JEOL SEM used for EDX. The GIWAXS measurements were performed on
7 the Sheffield Xeuss 2.0 instrument, and we are indebted to Xenocs for their ongoing help and support in
8 the user program at The University of Sheffield. We further thank Dr Sandra van Meurs of University of
9 Sheffield for assistance with the NMR spectroscopy measurements and analysis. We thank Claire
0 Greenland for useful discussions and feedback on the manuscript.

6 References

- 1 A. Kojima, K. Teshima, Y. Shirai and T. Miyasaka, *J. Am. Chem. Soc.*, 2009, **131**, 6050–6051.
- 2 M. A. Green, A. Ho-Baillie and H. J. Snaith, *Nat. Photonics*, 2014, **8**, 506–514.
- 3 G. Li, M. Price and F. Deschler, *APL Mater.*, 2016, **4**, 091507.
- 4 M. Ahmadi, T. Wu and B. Hu, *Adv. Mater.*, 2017, **29**, 1605242.
- 5 C. Bracher, B. G. Freestone, D. K. Mohamad, J. A. Smith and D. G. Lidzey, *Energy Sci. Eng.*, 2018, **6**, 35–46.
- 6 S. Luo and W. a Daoud, *J. Mater. Chem. A*, 2014, **00**, 1–19.
- 7 N. Aristidou, C. Eames, I. Sanchez-molina, X. Bu, J. Kosco, M. S. Islam and S. A. Haque, *Nat. Commun.*, 2017, **8**, 1–40.
- 8 B. Conings, J. Drijkoningen, N. Gauquelin, A. Babayigit, J. D’Haen, L. D’Olieslaeger, A. Ethirajan, J. Verbeeck, J. Manca, E. Mosconi, F. De Angelis and H. H.-G. Boyen, *Adv. Energy Mater.*, 2015, **5**, 1500477.
- 9 I. C. Smith, E. T. Hoke, D. Solis-Ibarra, M. D. McGehee and H. I. Karunadasa, *Angew. Chemie - Int. Ed.*, 2014, **53**, 11232–11235.
- 10 H. Tsai, W. Nie, J.-C. Blancon, C. C. Stoumpos, R. Asadpour, B. Harutyunyan, A. J. Neukirch, R. Verduzco, J. Crochet, S. Tretiak, L. Pedesseau, J. Even, M. A. Alam, G. Gupta, J. Lou, P. M. Ajayan, M. J. Bedzyk, M. G. Kanatzidis and A. D. Mohite, *Nature*, 2016, **536**, 312–316.
- 11 A. Vassilakopoulou, D. Papadatos, I. Zakouras and I. Koutselas, *J. Alloys Compd.*, 2017, **692**, 589–598.
- 12 T. Kataoka, T. Kondo, R. Ito, S. Sasaki, K. Uchida and N. Miura, *Phys. B Condens. Matter*, 1993, **184**, 132–136.
- 13 K. Tanaka, T. Takahashi, T. Kondo, T. Umebayashi, K. Asai and K. Ema, *Phys. Rev. B - Condens. Matter Mater. Phys.*, 2005, **71**, 1–6.
- 14 G. Grancini, C. Roldán-Carmona, I. Zimmermann, E. Mosconi, X. Lee, D. Martineau, S. Narbey, F. Oswald, F. De Angelis, M. Graetzel and M. K. Nazeeruddin, *Nat. Commun.*, 2017, **8**, 1–8.
- 15 A. Mei, X. Li, L. Liu, Z. Ku, T. Liu, Y. Rong, M. M. Xu, M. Hu, J. Chen, Y. Yang, M. Grätzel, H. Han, M. Gratzel and H. Han, *Science (80-.)*, 2014, **345**, 295–298.
- 16 Z. Wang, Q. Lin, F. P. Chmiel, N. Sakai, L. M. Herz and H. J. Snaith, *Nat. Energy*, 2017, 1–16.

- 1 17 L. Mao, W. Ke, L. Pedesseau, Y. Wu, C. Katan, J. Even, M. R. Wasielewski, C. C. Stoumpos and M. G.
2 Kanatzidis, *J. Am. Chem. Soc.*, 2018, **140**, 3775–3783.
- 3 18 C. M. M. Soe, C. C. Stoumpos, M. Kepenekian, B. Traoré, H. Tsai, W. Nie, B. Wang, C. Katan, R. Seshadri,
4 A. D. Mohite, J. Even, T. J. Marks and M. G. Kanatzidis, *J. Am. Chem. Soc.*, 2017, **139**, 16297–16309.
- 5 19 C. C. Stoumpos, D. H. Cao, D. J. Clark, J. Young, J. M. Rondinelli, J. I. Jang, J. T. Hupp and M. G. Kanatzidis,
6 *Chem. Mater.*, 2016, **28**, 2852–2867.
- 7 20 M. E. Kamminga, H.-H. Fang, M. R. Filip, F. Giustino, J. Baas, G. R. Blake, M. A. Loi and T. T. M. Palstra,
8 *Chem. Mater.*, 2016, **28**, 4554–4562.
- 9 21 Z. Song, S. C. Watthage, A. B. Phillips, B. L. Tompkins, R. J. Ellingson and M. J. Heben, *Chem. Mater.*, 2015,
0 **27**, 4612–4619.
- 1 22 M. L. Petrus, Y. Hu, D. Moia, P. Calado, A. M. A. Leguy, P. R. F. Barnes and P. Docampo, *ChemSusChem*,
2 2016, **9**, 2699–2707.
- 3 23 B. W. Park, B. Philippe, T. Gustafsson, K. Sveinbjörnsson, A. Hagfeldt, E. M. J. Johansson and G. Boschloo,
4 *Chem. Mater.*, 2014, **26**, 4466–4471.
- 5 24 M. I. Saidaminov, O. F. Mohammed and O. M. Bakr, *ACS Energy Lett.*, 2017, **2**, 889–896.
- 6 25 S. Tombe, G. Adam, H. Heilbrunner, C. Yumusak, D. H. Apaydin, B. Hailegnaw, C. Ulbricht, C. J. Arendse,
7 H. Langhals, E. Iwuohaa, N. S. Sariciftci and M. C. Scharber, *Sol. Energy*, 2018, **163**, 215–223.
- 8 26 Y. Yang, S. Feng, M. Li, W. Xu, G. Yin, Z. Wang, B. Sun and X. Gao, *Sci. Rep.*, 2017, **7**, 1–9.
- 9 27 E. M. Alexeev, A. Catanzaro, O. V. Skrypka, P. K. Nayak, S. Ahn, S. Pak, J. Lee, J. I. Sohn, K. S. Novoselov, H.
0 S. Shin and A. I. Tartakovskii, *Nano Lett.*, 2017, **17**, 5342–5349.
- 1 28 R. L. Milot, R. J. Sutton, G. E. Eperon, A. A. Haghighirad, J. Martinez Hardigree, L. Miranda, H. J. Snaith, M.
2 B. Johnston and L. M. Herz, *Nano Lett.*, 2016, **16**, 7001–7007.
- 3 29 D. H. Cao, C. C. Stoumpos, O. K. Farha, J. T. Hupp and M. G. Kanatzidis, *J. Am. Chem. Soc.*, 2015, **137**,
4 7843–7850.
- 5 30 M. Li, W. Xu, B. Sun, G. Yin, Z. Wang, X. Gao, S. Feng and Y. Yang, *Sci. Rep.*, 2017, **7**, 1–9.
- 6 31 A. T. Barrows, S. Lilliu, A. J. Pearson, D. Babonneau, A. D. F. Dunbar and D. G. Lidzey, *Adv. Funct. Mater.*,
7 2016, **26**, 4934–4942.

- 1 32 S. Lilliu, T. G. Dane, M. Alsari, J. Griffin, A. T. Barrows, M. S. Dahlem, R. H. Friend, D. G. Lidzey and J. E.
2 Macdonald, *Adv. Funct. Mater.*, 2016, **26**, 8221–8230.
- 3 33 D. K. Mohamad, B. G. Freestone, R. Masters, M. Reinhardt, S. Canning, C. Rodenburg and D. G. Lidzey, *J.*
4 *Mater. Chem. C*, 2017, **5**, 2352–2359.
- 5 34 D. P. McMeekin, Z. Wang, W. Rehman, F. Pulvirenti, J. B. Patel, N. K. Noel, M. B. Johnston, S. R. Marder,
6 L. M. Herz and H. J. Snaith, *Adv. Mater.*, 2017, **29**, 229–255.
- 7 35 W. Ke, I. Spanopoulos, C. C. Stoumpos and M. G. Kanatzidis, *Nat. Commun.*, 2018, **9**, 4785.
- 8 36 N. K. Noel, M. Congiu, A. J. Ramadan, S. Fearn, P. David, J. B. Patel, M. B. Johnston, B. Wenger and H. J.
9 Snaith, *Joule*, 2017, **1**, 328–343.
- 0 37 B. Dou, L. M. Wheeler, J. A. Christians, D. T. Moore, S. P. Harvey, J. J. Berry, F. S. Barnes, S. E. Shaheen
1 and M. F. A. M. Van Hest, *ACS Energy Lett.*, 2018, **3**, 979–985.
- 2 38 W. Franssen, B. Bruijnaers, V. Portengen and A. Kentgens, *ChemPhysChem*, 2018, 3107–3115.
- 3 39 J. H. Noh, S. H. Im, J. H. Heo, T. N. Mandal and S. Il Seok, *Nano Lett.*, 2013, **13**, 1764–1769.
- 4 40 J. S. Manser, M. I. Saidaminov, J. A. Christians, O. M. Bakr and P. V. Kamat, *Acc. Chem. Res.*, 2016, **49**,
5 330–338.
- 6 41 J. B. Patel, R. L. Milot, A. D. Wright, L. M. Herz and M. B. Johnston, *J. Phys. Chem. Lett.*, 2016, **7**, 96–102.
- 7 42 Y. Hu, T. Bein, P. Docampo, M. van Schilfgaarde, M. Campoy-Quiles, M. T. Weller, P. Azarhoosh, A. M. A.
8 Leguy, M. I. Alonso, O. J. Weber, P. R. F. Barnes and J. Nelson, *Chem. Mater.*, 2015, **27**, 3397–3407.
- 9 43 G. C. Papavassiliou, *Prog. Solid State Chem.*, 1997, **25**, 125–270.
- 0 44 T. Ishihara, *J. Lumin.*, 1994, **60–61**, 269–274.
- 1 45 G. H. Imler, X. Li, B. Xu, G. E. Dobereiner, H.-L. Dai, Y. Rao and B. B. Wayland, *Chem. Commun.*, 2015, **51**,
2 11290–11292.
- 3 46 B. R. Vincent, K. N. Robertson, T. S. Cameron and O. Knop, *Can. J. Chem.*, 2006, **65**, 1042–1046.
- 4 47 G. Tang, C. Yang, A. Stroppa, D. Fang and J. Hong, *J. Chem. Phys.*, 2017, **146**, 224702.
- 5 48 A. A. Petrov, I. P. Sokolova, N. A. Belich, G. S. Peters, P. V. Dorovatovskii, Y. V. Zubavichus, V. N.
6 Khrustalev, A. V. Petrov, M. Grätzel, E. A. Goodilin and A. B. Tarasov, *J. Phys. Chem. C*, 2017, **121**, 20739–
7 20743.

- 1 49 A. T. Barrows, S. Lilliu, A. J. Pearson, D. Babonneau, A. D. F. Dunbar and D. G. Lidzey, *Adv. Funct. Mater.*,
2 2016, **26**, 4934–4942.
- 3 50 K. H. Stone, A. Gold-Parker, V. L. Pool, E. L. Unger, A. R. Bowring, M. D. McGehee, M. F. Toney and C. J.
4 Tassone, *Nat. Commun.*, 2018, **9**, 3458.
- 5 51 B. Palosz, *J. Phys. Condens. Matter*, 1990, **2**, 5285–5295.
- 6 52 R. J. D. Tilley, *Perovskites: Structure–Property Relationships*, John Wiley & Sons, Ltd, Chichester, UK,
7 2016, vol. 42.
- 8 53 K. Momma and F. Izumi, *J. Appl. Crystallogr.*, 2011, **44**, 1272–1276.
- 9 54 J. P. Perdew, A. Ruzsinszky, G. I. G. I. Csonka, O. A. Vydrov, G. E. Scuseria, L. A. Constantin, X. Zhou and K.
0 Burke, *Phys. Rev. Lett.*, 2008, **100**, 136406.
- 1 55 M. Dion, H. Rydberg, E. Schröder, D. C. Langreth and B. I. Lundqvist, *Phys. Rev. Lett.*, 2004, **92**, 22–25.
- 2 56 F. Brivio, A. B. Walker and A. Walsh, *APL Mater.*, 2013, **1**, 042111.
- 3 57 A. Stroppa, D. Di Sante, P. Barone, M. Bokdam, G. Kresse, C. Franchini, M.-H. Whangbo and S. Icozzi, *Nat.*
4 *Commun.*, 2014, **5**, 1–8.
- 5 58 I. E. Castelli, J. M. García-Lastra, K. S. Thygesen and K. W. Jacobsen, *APL Mater.*, 2014, **2**, 081514.
- 6 59 A. M. Ganose, C. N. Savory and D. O. Scanlon, *J. Phys. Chem. Lett.*, 2015, **6**, 4594–4598.
- 7 60 F. Brivio, J. M. Frost, J. M. Skelton, A. J. Jackson, O. J. Weber, M. T. Weller, A. R. Goñi, A. M. A. Leguy, P. R.
8 F. Barnes and A. Walsh, *Phys. Rev. B*, 2015, **92**, 144308.
- 9 61 S. F. Yuk, K. C. Pitike, S. M. Nakhmanson, M. Eisenbach, Y. W. Li and V. R. Cooper, *Sci. Rep.*, 2017, **7**,
0 43482.
- 1 62 B. Traore, L. Pedesseau, L. Assam, X. Che, J. C. Blancon, H. Tsai, W. Nie, C. C. Stoumpos, M. G. Kanatzidis,
2 S. Tretiak, A. D. Mohite, J. Even, M. Kepenekian and C. Katan, *ACS Nano*, 2018, **12**, 3321–3332.
- 3 63 M. Kepenekian, B. Traore, J.-C. C. Blancon, L. Pedesseau, H. Tsai, W. Nie, C. C. Stoumpos, M. G.
4 Kanatzidis, J. Even, A. D. Mohite, S. Tretiak and C. Katan, *Nano Lett.*, 2018, **18**, 5603–5609.
- 5 64 Y. Zhang, P. Wang, M. C. Tang, D. Barrit, W. Ke, J. Liu and T. Luo, *J. Am. Chem. Soc.*, 2019, 1–6.
- 6 65 O. Nazarenko, M. R. Kotyrba, M. Wörle, E. Cuervo-Reyes, S. Yakunin and M. V. Kovalenko, *Inorg. Chem.*,
7 2017, **56**, 11552–11564.

- 1 66 M. I. Dar, G. Jacopin, S. Meloni, A. Mattoni, N. Arora, A. Boziki, S. M. Zakeeruddin, U. Rothlisberger and
2 M. Grätzel, *Sci. Adv.*, 2016, **2**, e1601156.
- 3 67 K. Jemli, H. Diab, F. Lédée, G. Trippé-Allard, D. Garrot, B. Geffroy, J.-S. Lauret, P. Audebert and E.
4 Deleporte, *Molecules*, 2016, **21**, 885.
- 5 68 J. F. Condeles, R. A. Ando and M. Mulato, *J. Mater. Sci.*, 2008, **43**, 525–529.
- 6 69 K. Wu, A. Bera, C. Ma, Y. Du, Y. Yang, L. Li and T. Wu, *Phys. Chem. Chem. Phys.*, 2014, **16**, 22476–22481.
- 7 70 D. Meggiolaro, S. Motti, E. Mosconi, A. barker, J. Ball, C. A. R. Perini, F. Deschler, A. Petrozza and F. De
8 Angelis, *Energy Environ. Sci.*, 2018, **11**, 702–713.
- 9 71 Q. Shang, Y. Wang, Y. Zhong, Y. Mi, L. Qin, Y. Zhao, X. Qiu, X. Liu and Q. Zhang, *J. Phys. Chem. Lett.*, 2017,
0 **8**, 4431–4438.
- 1 72 N. Mercier, S. Poiroux, A. Riou and P. Batail, *Inorg. Chem.*, 2004, **43**, 8361–8366.
- 2 73 D. Papadatos, A. Vassilakopoulou and I. Koutselas, *J. Lumin.*, 2017, **188**, 567–576.
- 3 74 D. B. Mitzi, D. R. Medeiros and P. R. L. Malenfant, *Inorg. Chem.*, 2002, **41**, 2134–2145.
- 4 75 J.-C. Blancon, H. Tsai, W. Nie, C. C. Stoumpos, L. Pedesseau, C. Katan, M. Kepenekian, C. M. M. Soe, K.
5 Appavoo, M. Y. Sfeir, S. Tretiak, P. M. Ajayan, M. G. Kanatzidis, J. Even, J. J. Crochet and A. D. Mohite,
6 *Science (80-.)*, 2017, **355**, 1288–1292.
- 7 76 K. Z. Du, Q. Tu, X. Zhang, Q. Han, J. Liu, S. Zauscher and D. B. Mitzi, *Inorg. Chem.*, 2017, **56**, 9291–9302.
- 8 77 L. Ni, U. Huynh, A. Cheminal, T. H. Thomas, R. Shivanna, T. F. Hinrichsen, S. Ahmad, A. Sadhanala and A.
9 Rao, *ACS Nano*, 2017, **11**, 10834–10843.
- 0 78 L. D. Whalley, J. M. Skelton, J. M. Frost and A. Walsh, *Phys. Rev. B*, 2016, **94**, 220301.
- 1 79 X. Yang, X. Zhang, J. Deng, Z. Chu, Q. Jiang, J. Meng, P. Wang, L. Zhang, Z. Yin and J. You, *Nat. Commun.*,
2 2018, **9**, 2–9.
- 3 80 M. Yuan, L. N. Quan, R. Comin, G. Walters, R. Sabatini, O. Voznyy, S. Hoogland, Y. Zhao, E. M. Beauregard,
4 P. Kanjanaboos, Z. Lu, D. H. Kim and E. H. Sargent, *Nat. Nanotechnol.*, 2016, **11**, 872–877.
- 5 81 X. Hong, T. Ishihara and A. V. Nurmikko, *Phys. Rev. B*, 1992, **45**, 6961–6964.
- 6 82 Y. Tabuchi, K. Asai, M. Rikukawa, K. Sanui and K. Ishigure, *J. Phys. Chem. Solids*, 2000, **61**, 837–845.
- 7 83 R. L. Milot, G. E. Eperon, H. J. Snaith, M. B. Johnston and L. M. Herz, *Adv. Funct. Mater.*, 2015, **25**, 6218–

1 6227.

2 84 G. E. Eperon, S. D. Stranks, C. Menelaou, M. B. Johnston, L. M. Herz and H. J. Snaith, *Energy Environ. Sci.*,
3 2014, **7**, 982.

4 85 H. Yu, F. Wang, F. Xie, W. Li, J. Chen and N. Zhao, *Adv. Funct. Mater.*, 2014, **24**, 7102–7108.

5 86 Z. Jiang, *J. Appl. Crystallogr.*, 2015, **48**, 917–926.

6 87 M. Piotto, M. Bourdonneau, K. Elbayed, J.-M. Wieruszkeski and G. Lippens, *Magn. Reson. Chem.*, 2006, **44**,
7 943–947.

8 88 A. García, J. D. Gale, J. M. Soler, D. Sánchez-Portal, E. Artacho, P. Ordejón and J. Junquera, *J. Phys.*
9 *Condens. Matter*, 2002, **14**, 2745–2779.

0 89 E. Artacho, J. D. Gale, A. Garc, J. Junquera, R. M. Martin, P. Ordej, S.-P. Daniel and J. M. Soler, SIESTA 4.0
1 User's Guide.

2 90 SIESTA database (pseudopotentials and basis sets), <https://departments.icmab.es/leem/siesta/>,
3 (accessed 31 January 2019).

4